Enhanced Andronov–Hopf Oscillator Grid-Forming Inverters with Voltage-Independent Active-Power Droop Coefficient

Hamed Rezazadeh, Mohammad Monfared, *Senior Member, IEEE,*
Meghdad Fazeli, *Senior Member, IEEE*, and Saeed Golestan, *Senior Member, IEEE*

***Abstract*— Virtual oscillator control (VOC), particularly the Andronov–Hopf oscillator (AHO), has emerged as a promising grid-forming (GFM) strategy due to its fast transient response and inherent synchronisation capability. However, in conventional AHO-based inverters, the active power droop coefficient is inherently dependent on the voltage amplitude, which degrades frequency support under grid disturbances and leads to power-sharing inaccuracies. This paper proposes an enhanced AHO (EAHO) control strategy that achieves a voltage-independent active power droop coefficient while preserving the original AHO structure and its favourable dynamic characteristics. The proposed modification enhances frequency and voltage support, improves active and reactive power support, ensures accurate power sharing in stand-alone parallel operation with other GFM inverters, and enhances stability under severe grid voltage sags. Large-signal and small-signal analysis, as well as comprehensive experimental validation on 2.5 kVA single-phase inverters, confirm the superior steady-state performance, improved grid-support capability, and robust stability of the proposed EAHO under wide-ranging grid conditions.**

***Index Terms*— Andronov-Hopf Oscillator (AHO), grid-forming (GFM) inverter, virtual oscillator control (VOC).**

I. INTRODUCTION

WITH the growing dominance of inverter-based resources in modern power systems, grid-forming (GFM) inverters have gained considerable attention for their critical role in maintaining system stability and resilience. A common GFM approach involves synchronous generator (SG) emulation-based methods, which provide grid frequency and voltage support, as well as communication-free power-sharing, by emulating the behaviour of SGs. These methods include droop control [1], virtual synchronous generator [2], [3], synchronverter [4], [5], and synchronous power control [6]. All these strategies incorporate droop functionality, where the angular frequency (ω) and amplitude (V_p) of the inverter's voltage are linear functions of active (P) and reactive (Q) powers, respectively.

To improve the dynamic response of the SG-emulation-based methods, virtual oscillator control (VOC) has been proposed as an emerging GFM strategy. VOC leverages the synchronisation behaviour of coupled oscillator networks, allowing the system to quickly stabilise to a limit cycle [7], [8]. VOC inherently stabilises arbitrary initial conditions to a sinusoidal steady state. Thus, it achieves global asymptotic synchronisation and enhanced transient performance compared to traditional droop control [9]. Furthermore, VOC's control strategy relies directly on the inverter output current, eliminating the need for power measurements and low-pass filtering, thereby further improving transient speed and power-sharing dynamics [10], [11]. Among various VOC implementations, the Andronov-Hopf oscillator (AHO) stands out for its dispatchability and ability to generate a harmonic-free voltage waveform [12], [13], [14].

Recently, the AHO has been equipped with virtual inertia, increasing its relevance in modern power systems, although at the cost of reduced damping [15], [16]. To address this issue, two recent damping enhancement methods have been proposed [17], [18]. Additionally, a new control strategy in the dq reference frame has been developed to enhance the power tracking and dynamic response of the VOC [19].

Despite these advantages, the droop coefficients of the AHO are nonlinear functions of the voltage amplitude V_p. In particular, the active power loop (APL) droop coefficient, unlike in conventional SG emulation-based methods, varies with V_p, complicating the design of control parameters, as they must account for the allowable range of V_p. As a result, the inverter's ability to provide consistent grid support during frequency disturbances can be compromised. Moreover, power-sharing inaccuracies may arise when AHO-based inverters operate in parallel with other GFM units.

This paper proposes an enhanced AHO (EAHO) control strategy that achieves a voltage-independent active-power droop coefficient, while preserving the AHO's core structure and its fast dynamics. The proposed strategy improves grid support capabilities in response to fluctuations in both grid frequency and voltage amplitude, ensures accurate power-sharing in stand-alone mode, even when operating in parallel with other GFM strategies, and enhances large-signal stability under sever grid voltage disturbances. Here, the EAHO is designed for single-phase applications to address a gap arising

---

Manuscript received Month xx, 2xxx; revised Month xx, xxxx; accepted Month x, xxxx. (Corresponding author: Mohammad Monfared.)

Hamed Rezazadeh, Mohammad Monfared and Meghdad Fazeli are with the Department of Electronic and Electrical Engineering, Swansea University, SA1 8EN Swansea, U.K. (e-mail: 2251309@swansea.ac.uk; mohammad.monfared@swansea.ac.uk; m.fazeli@swansea.ac.uk).

Saeed Golestan is with AAU Energy, Aalborg University, 9220 Aalborg East, Denmark (e-mail: sgd@energy.aau.dk).

from the increasing deployment of small-scale distributed generation in residential and commercial areas, mainly rooftop solar PVs and energy storage systems, which necessitate the use of single-phase GFM inverters to ensure safe and stable operation of inverter-based resources [20], [21], [22]. Nevertheless, the strategy is scalable and applicable to three-phase systems. Furthermore, although the focus is on ω-P and V_p-Q droop functionality, the proposed strategy is also compatible with dominantly resistive systems with ω-Q and V_p-P droop. The effectiveness of the proposed strategy is demonstrated through large-signal and small-signal analysis with experimental validation on 2.5 kVA single-phase inverters in both grid-connected and stand-alone modes.

The rest of this paper is organised as follows: Section II reviews the conventional AHO and introduces the proposed EAHO strategy, accompanied by a comprehensive analysis and a small-signal state-space and large-signal stability investigation. Section III presents the experimental validation, and Section IV concludes the paper.

II. CONVENTIONAL AND ENHANCED AHO

A. Conventional AHO

The AHO is a time-domain controller implemented in the $\alpha\beta$ reference frame. The control law for the oscillator output voltage is expressed as:

$$\dot{v} = \underbrace{j\omega_0 v}_{1} + \underbrace{\mu\left(V_{p0}^2 - V_p^2\right)v}_{2} + \underbrace{j\,\eta(i_{ref} - i)}_{3} \tag{1}$$

where v is the oscillator output voltage, ω_0 and V_{p0} represent the nominal values for angular frequency (ω) and voltage vector magnitude (V_p), i_{ref} is the reference value of the inverter's output current (i), and η and μ are AHO's control parameters [12]. This equation illustrates that the AHO dynamics consist of three terms: (1) the harmonic oscillator, (2) the voltage magnitude correction, and (3) the synchronisation feedback (current input) [12]. Equation (1) can be rewritten in the $\alpha\beta$ reference frame as:

$$\begin{bmatrix}\dot{v}_\alpha\\ \dot{v}_\beta\end{bmatrix} = \begin{bmatrix}\mu\left(V_{p0}^2 - V_p^2\right) & -\omega_0\\ \omega_0 & \mu\left(V_{p0}^2 - V_p^2\right)\end{bmatrix}\begin{bmatrix}v_\alpha\\ v_\beta\end{bmatrix} + \eta\begin{bmatrix}0 & -1\\ 1 & 0\end{bmatrix}\begin{bmatrix}i_{\alpha ref} - i_\alpha\\ i_{\beta ref} - i_\beta\end{bmatrix} \tag{2}$$

where v_α and v_β are the oscillator output voltages, $i_{\alpha ref}$ and $i_{\beta ref}$ are the inverter's reference currents, and i_α and i_β denote the inverter's output currents in the $\alpha\beta$ reference frame. In single-phase systems, since only the α-axis current is physically available, the current component i_β is usually generated by a second-order generalised integrator-based quadrature signal generator (SOGI-QSG) [23].

The time derivatives of the oscillator voltage amplitude ($V_p = \sqrt{v_\alpha^2 + v_\beta^2}$) and phase ($\theta$=arctan($v_\beta/v_\alpha$)) are given by:

$$\begin{cases}\dot{V}_p = \dfrac{v_\alpha\dot{v}_\alpha + v_\beta\,\dot{v}_\beta}{V_p}\\[2ex] \dot{\theta} = \dfrac{\dot{v}_\beta v_\alpha - \dot{v}_\alpha v_\beta}{V_p^2}.\end{cases} \tag{3}$$

Substituting (2) into (3) yields:

$$\begin{cases}\dot{V}_p = \mu\left(V_{p0}^2 - V_p^2\right)V_p + \dfrac{2\eta}{V_p}\left(Q_{ref} - Q\right)\\[2ex] \dot{\theta} = \omega = \omega_0 + \dfrac{2\eta}{V_p^2}\left(P_{ref} - P\right)\end{cases} \tag{4}$$

where P_{ref} and Q_{ref} are the reference values of the active and reactive powers, respectively. As seen from (4), the oscillator's voltage amplitude evolves dynamically until equilibrium is reached ($\dot{V}_p$=0). At this steady state, the droop characteristics of AHO can be obtained as shown in (5).

$$\begin{cases}V_p^4 = V_{p0}^2V_p^2 + \dfrac{2\eta}{\mu}\left(Q_{ref} - Q\right)\\[2ex] \omega = \omega_0 + \dfrac{2\eta}{V_p^2}\left(P_{ref} - P\right)\end{cases} \tag{5}$$

The APL and reactive power loop (RPL) droop coefficients, m_p and m_q, are defined as [9]:

$$\begin{cases}m_p = -\dfrac{d\omega}{dP}\\[2ex] m_q = -\dfrac{dV_p}{dQ} = -\dfrac{1}{\dfrac{dQ}{dV_p}}.\end{cases} \tag{6}$$

Substituting (5) into (6) yields:

$$\begin{cases}m_{p,AHO} = \dfrac{2\eta}{V_p^2}\\[2ex] m_{q,AHO} = \dfrac{\eta}{\mu V_p\left(2V_p^2 - V_{p0}^2\right)}\end{cases} \tag{7}$$

where $m_{p,AHO}$ and $m_{q,AHO}$ are the AHO's droop coefficients. From (7), it is evident that $m_{p,AHO}$ is inversely proportional to the square of the voltage amplitude V_p. Furthermore, the expression for $m_{q,AHO}$ becomes negative when $V_p < V_{p0}/\sqrt{2}$, which can jeopardise system stability.

According to the droop control principle, powers should reach their nominal values (P_0 and Q_0) in response to the maximum allowable frequency deviation ($\Delta\omega_{max}$) and voltage amplitude ($V_{p,max}$), respectively. Substituting these conditions into (5) gives the control parameters as [12]:

$$\eta = \frac{\Delta\omega_{max}V_{p,max}^2}{2P_0}, \quad \mu = \frac{2\eta Q_0}{V_{p,max}^4 - V_{p0}^2V_{p,max}^2}. \tag{8}$$

B. Enhanced AHO

Fig. 1 illustrates the proposed EAHO-based GFM scheme for a single-phase inverter, where L_f, R_f, and C_f denote the filter inductance, its parasitic resistance, and the filter capacitance, respectively. Z_L is the local load, and L_g and R_g represent the grid impedance. In this configuration, V_{dc} is the DC-link voltage and v_{pcc} represents the voltage at the point of common coupling.

As already stated in [24], any change to the first two terms of (1) compromises the fast dynamic response and low harmonic distortion of the AHO. Thus, in this work, only the third term is manipulated through multiplying the current error by $V_p^2/2$, as

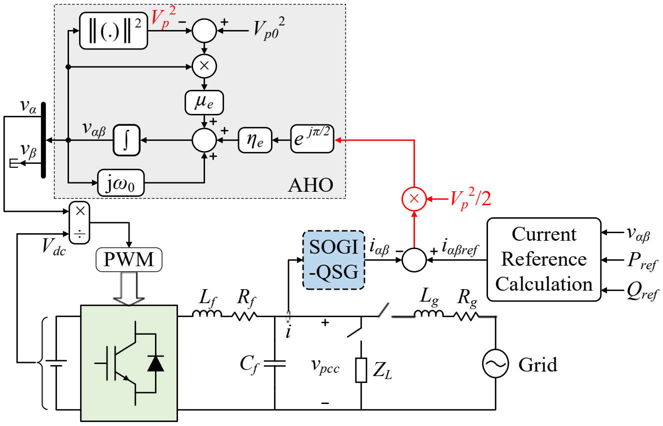

Fig. 1. Proposed EAHO-based single-phase GFM inverter.

highlighted in Fig. 1. The control law of the EAHO can then be expressed as:

$$\begin{bmatrix}\dot{v}_\alpha\\ \dot{v}_\beta\end{bmatrix}=\begin{bmatrix}\mu_e\left(V_{p0}^2-V_p^2\right) & -\omega_0\\ \omega_0 & \mu_e\left(V_{p0}^2-V_p^2\right)\end{bmatrix}\begin{bmatrix}v_\alpha\\ v_\beta\end{bmatrix}+\eta_e\frac{V_p^2}{2}\begin{bmatrix}0 & -1\\ 1 & 0\end{bmatrix}\begin{bmatrix}i_{\alpha ref}-i_\alpha\\ i_{\beta ref}-i_\beta\end{bmatrix} \tag{9}$$

where η_e and μ_e are the EAHO's control parameters. The modification term introduced in (9) is based on the idea of feedback linearisation in nonlinear control. Feedback linearisation is a common nonlinear control strategy that transforms a nonlinear system into an equivalent linear one by changing variables and/or applying a suitable control input [25]. From a physical perspective, this modification can be interpreted as a normalisation of the control action with respect to the voltage magnitude. Comparing (2) and (9) shows that the first terms are identical, while the current error term has been modified to achieve the APL droop coefficient independent of the voltage. Substituting (9) into (3) results in:

$$\begin{cases}\dot{V}_p=\mu_e\left(V_{p0}^2-V_p^2\right)V_p+\eta_e V_p\left(Q_{ref}-Q\right)\\ \dot{\theta}=\omega=\omega_0+\eta_e\left(P_{ref}-P\right).\end{cases} \tag{10}$$

At equilibrium ($\dot{V}_p$=0), the droop characteristics of EAHO can be obtained as (11).

$$\begin{cases}V_p^2=V_{p0}^2+\dfrac{\eta_e}{\mu_e}\left(Q_{ref}-Q\right)\\ \omega=\omega_0+\eta_e\left(P_{ref}-P\right)\end{cases} \tag{11}$$

As shown in (11), the proposed modification leads to a linear APL droop equation that is independent of V_p. Additionally, the RPL droop reduces to a quadratic voltage dependence, rather than the quartic dependence observed in the AHO. Similar to the AHO, the EAHO control parameters η_e and μ_e should be designed such that the active and reactive powers reach their nominal values at the maximum allowable grid frequency deviation and maximum voltage amplitude, respectively. These parameters can thus be determined from (11), as given in (12).

$$\eta_e=\frac{\Delta\omega_{max}}{P_0},\quad \mu_e=\frac{\eta_e Q_0}{V_{p,max}^2-V_{p0}^2} \tag{12}$$

TABLE I

EXPERIMENTAL PARAMETERS

Parameters	Description	Value
P_0, Q_0	rated active and reactive power	2000 W, 1500 var
V_{dc}	DC-link voltage	380 V
ω_0	nominal angular frequency	2π × 50 rad/s
V_{p0}	nominal voltage amplitude	311 V
L_f, C_f	filter impedance	7 mH, 3.9 μF
L_g, R_g	grid impedance	1 mH, 1 Ω
η, μ	AHO control parameters	91.99, 1.16×10^{-4}
η_e, μ_e	EAHO control parameters	0.0016, 1.16×10^{-4}
$m_{p,droop}$, $m_{q,droop}$	droop control parameters	0.0016, 0.0207

These expressions show that, similar to the AHO, the EAHO's controller parameters are determined from grid code requirements and inverter ratings. According to the National Grid Electricity System Operator for Great Britain, the maximum allowable frequency deviation is ±0.5 Hz (i.e., Δf_{max}=0.01 pu) [26]. Additionally, the typical voltage tolerance is up to 110% of the nominal value. Therefore, the control parameters for both the conventional and proposed strategies are selected using equations (8) and (12) and are summarised in Table I to satisfy these requirements.

The EAHO's droop coefficients can be calculated by substituting (11) into (6), resulting in:

$$\begin{cases}m_{p,EAHO}=\eta_e\\ m_{q,EAHO}=\dfrac{\eta_e}{2\mu_e V_p}\end{cases} \tag{13}$$

where $m_{p,EAHO}$ and $m_{q,EAHO}$ are the droop coefficients under the EAHO strategy. Equation (13) shows that the APL droop coefficient simplifies to η_e, making it independent of voltage magnitude. Additionally, in contrast to the AHO case, $m_{q,EAHO}$ remains positive for all V_p, thus improving RPL's stability under varying grid conditions.

Fig. 2 illustrates the variation of the active power droop coefficient as a function of the voltage amplitude V_p for both the conventional AHO and the proposed EAHO using the parameters listed in Table I. It can be observed that the droop coefficient of the conventional AHO is inversely proportional to V_p, resulting in a noticeable variation as the voltage amplitude changes. In contrast, the EAHO maintains a constant droop coefficient over the entire operating range, confirming its independence from voltage amplitude. This characteristic ensures consistent frequency support and improves power-sharing accuracy under varying voltage conditions.

In addition to enhancing the APL droop, the proposed strategy also improves the reactive power support capability compared to the conventional AHO. By defining $\delta=\theta-\theta_g$ as the phase angle difference between the oscillator voltage and grid voltage, the dynamic equations of EAHO, as given in (10), simplify to:

$$\begin{cases}\dot{V}_p=\mu_e\left(V_{p0}^2-V_p^2\right)V_p+\eta_e V_p\left(Q_{ref}-Q\right)\\ \dot{\delta}=\eta_e\left(P_{ref}-P\right)\end{cases} \tag{14}$$

For a single-phase inverter connected to a grid, the injected active and reactive powers from the inverter to the grid can be calculated as:

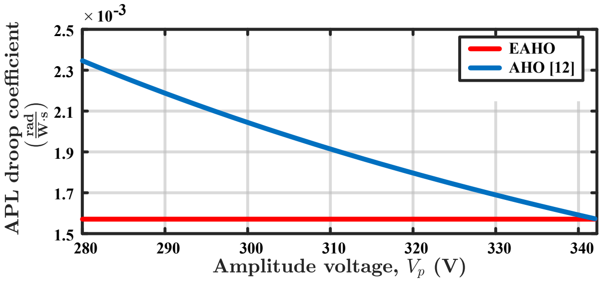

Fig. 2. Comparison of APL droop coefficients.

$$\begin{cases} P = \dfrac{R_T\left(V_p^2 - V_pV_g\, cos(\delta)\right) + X_TV_pV_g\, sin(\delta)}{2(R_T^2 + X_T^2)} \\ Q = \dfrac{X_T\left(V_p^2 - V_pV_g\, cos(\delta)\right) - R_TV_pV_g\, sin(\delta)}{2(R_T^2 + X_T^2)} \end{cases} \tag{15}$$

where R_T=R_f+R_g, X_T=X_f+X_g, and V_g is the grid amplitude voltage. These expressions confirm that both power components are inherently dependent on voltage magnitude and phase difference, as well as circuit parameters. However, the primary contribution of this paper is that the active power droop coefficient is no longer a function of the voltage amplitude and therefore not affected by its variations.

Substituting (15) into (14) yields a set of two nonlinear differential equations. These equations are solved numerically (using MATLAB) for the parameters given in Table I, assuming a 20% grid voltage drop, with P_{ref} = 0 W and Q_{ref} = 0. Under these conditions, the EAHO injects 1443 var of reactive power at steady-state. A similar large-signal analysis for the conventional AHO results in 1078 var. These results indicate that the proposed EAHO injects approximately 25% more reactive power than the conventional AHO, thereby offering enhanced grid support under voltage amplitude variations.

C. Power-sharing in Parallel Operation in Stand-Alone Mode

Consider a system with N parallel inverters supplying a local load in stand-alone operation. The inverters are controlled using EAHO, AHO, or droop control.

The droop control law is given in (16)

$$\begin{cases} V_p = V_{p0} + m_{q,droop}\left(Q_{ref} - Q_f\right) \\ \omega = \omega_0 + m_{p,droop}\left(P_{ref} - P_f\right) \end{cases} \tag{16}$$

where $m_{q,droop}$ and $m_{p,droop}$ are the RPL and APL droop coefficients, respectively, and Q_f and P_f are the measured reactive and active power filtered using a low-pass filter to mitigate measurement noises [1]. Similar to EAHO and AHO, the APL droop coefficient of the droop control should be designed such that active power reaches its nominal value (P_0) in response to the maximum allowable frequency deviation ($\Delta\omega_{max}$), as given in (17).

$$m_{p,droop} = \frac{\Delta\omega_{max}}{P_0} \tag{17}$$

Assuming P_{ref} = 0 in stand-alone mode, the steady-state frequency–power relationship for all GFM controllers can be expressed in a unified droop form as:

$$\omega_i = \omega_0 - m_{pi}P_i \tag{18}$$

where ω_i, m_{pi}, and P_i are the angular frequency, APL droop coefficient, and output active power of the i^{th} inverter, respectively. The APL droop coefficient, m_p, for the AHO, EAHO, and droop control are given in (7), (13), and (17), respectively. From the frequency synchronisation condition, we have $\omega_i = \omega_j$ (i,j=1,2,…,N). Thus,

$$\frac{P_i}{P_j} = \frac{m_{pj}}{m_{pi}}. \tag{19}$$

First, consider two inverters i and j controlled by EAHO and droop control, respectively. Substituting (12), (13), (17), and (18) into (19) yields:

$$\frac{P_i}{P_j} = \frac{m_{pj}}{m_{pi}} = \frac{m_{p,droop}}{\eta_e} = \frac{P_{0i}}{P_{0j}}. \tag{20}$$

Equation (20) shows that EAHO ensures power sharing proportional to the inverter ratings, which guarantees accurate load sharing. For identical ratings, equal power sharing is achieved. Next, consider an inverter k controlled by the conventional AHO operating in parallel with a droop-controlled inverter j. In this case:

$$\frac{P_k}{P_j} = \frac{m_{pj}}{m_{pk}} = \frac{m_{p,droop}}{2\eta/V_p^2} = \frac{P_{0k}}{P_{0j}} \times \frac{V_p^2}{V_{p,max}^2}. \tag{21}$$

This expression shows that, unlike EAHO, the power sharing of AHO depends not only on inverter ratings but also on the instantaneous voltage amplitude and its maximum allowable value. As a result, even for inverters with identical ratings, unequal power sharing occurs under voltage variations.

D. Small-Signal Stability Analysis

This section investigates the stability performance of the proposed EAHO. To this end, its small-signal model is derived in state-space form:

$$\Delta\dot{x} = A\,\Delta x + B\,\Delta u \tag{22}$$

where x is the state vector, u represents the system input, Δx is a small perturbation around the equilibrium point X_{eq}, and A and B are the Jacobian Matrices. The system is exponentially stable if all eigenvalues of matrix A lie in the left half of the complex plane. In the following, x_d and x_q denote the component of x projected onto the grid voltage's dq frame.

In the dq reference frame, the inverter's voltage components are defined as v_d=$V\cos(\theta)$ and v_q=$V\sin(\theta)$, where V=$V_p/\sqrt{2}$ is the RMS value of the voltage. Thus, for the single-phase inverter connected to the grid, the current dynamics and output power expressions in the dq frame are given by:

$$\begin{cases} \dot{i}_d = -\dfrac{R_T}{L_T}i_d + \omega i_q + \dfrac{V\cos(\theta)}{L_T} - \dfrac{V_g}{L_T} \\ \dot{i}_q = -\omega i_d - \dfrac{R_T}{L_T}i_q + \dfrac{V\sin(\theta)}{L_T} \end{cases} \tag{23}$$

$$\begin{cases} P = V\cos(\theta)\ i_d + V\sin(\theta)\ i_q \\ Q = V\sin(\theta)\ i_d - V\cos(\theta)\ i_q \end{cases} \tag{24}$$

The dynamic equations of the EAHO were previously derived in (10). By substituting (24) into (10) and linearising the resulting equations and (23) around the equilibrium point, a

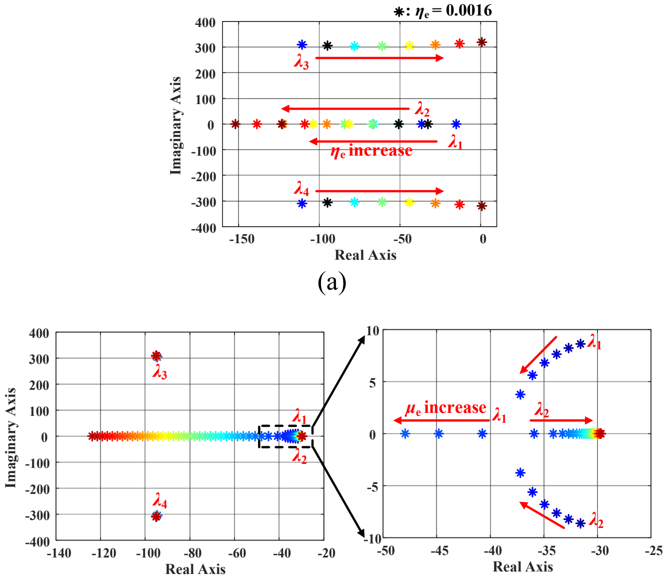

(a)

(b)

Fig. 3. Eigenvalue map of EAHO: (a) η_e changes from $0.5\eta_{e,set}$ to $4\eta_{e,set}$ and (b) μ_e changes from $0.1\mu_{e,set}$ to $4\mu_{e,set}$.

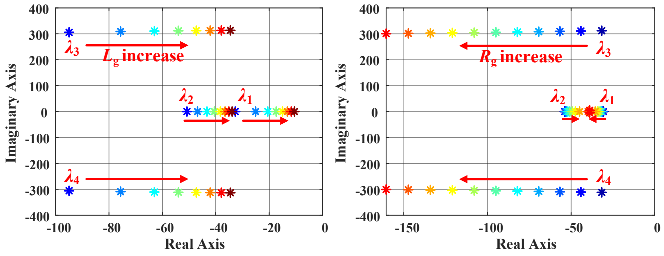

(a)

(b)

Fig. 4. Eigenvalue map of EAHO: (a) L_g changes from 1 mH to 15 mH and (b) R_g changes from 0.5 Ω to 1.5 Ω.

state-space representation as in (22) is obtained, where Δx=[Δv, $\Delta\theta$, Δi_d, Δi_q]^T and Δu=Δv_g. The resulting Jacobian matrix A is presented in (25), where the equilibrium point is given by X_{eq}=[V_{eq}, θ_{eq}, I_d, I_q]^T and ω_{eq}=ω_g. To determine X_{eq}, the steady-state conditions $\dot{i}_d=\dot{i}_q=\dot{V}=0$ are applied. The resulting nonlinear algebraic equations are solved using Newton's iteration method, implemented in MATLAB. For the experimental parameters listed in Table I, the equilibrium point is found to be: X_{eq} = [224.39 V, 0.1079 rad, 8.72 A, 2.24 A]^T.

Fig. 3 presents the eigenvalue loci of the linearised system in the complex plane for varying control parameters. Fig. 3(a) shows the eigenvalue map of the EAHO as η_e changes from $0.5\eta_{e,set}$ to $4\eta_{e,set}$, where $\eta_{e,set}$ = 0.0016 is the designed value that satisfies the grid requirements. This figure reveals that for small values of η_e, the dominant eigenvalues are λ_1 and λ_2, which move leftward, away from the imaginary axis, as η_e increases, indicating an improved dynamic response. However, for excessively large η_e, eigenvalues λ_3 and λ_4 become dominant and approach the imaginary axis, suggesting reduced stability margins. For this system, $\eta_e = 4\eta_{e,set}$ marks the critical threshold beyond which the system becomes unstable. The eigenvalues corresponding to $\eta_e = \eta_{e,set}$ (the value dictated by grid requirements), are marked with the black "*", confirming the stable operation of EAHO.

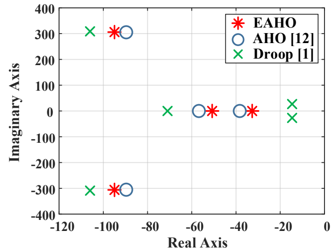

Fig. 5. Eigenvalue comparison.

Fig. 3(b) presents the eigenvalue map as μ_e changes from $0.1\mu_{e,set}$ to $4\mu_{e,set}$, where $\mu_{e,set}$ is the designed value. This figure reveals that the eigenvalues λ_3 and λ_4 change slightly with the change in μ_e. In contrast, λ_1 moves to the left and away from the imaginary axis by increasing μ_e, which implies a faster response. However, λ_2 first moves to the left for $0.1\mu_{e,set} < \mu_e < 0.6\mu_{e,set}$, then changes slightly with the increase of μ_e.

Fig. 4 analyses the performance of the proposed strategy under varying grid impedance. Fig. 4(a) presents the eigenvalue map when L_g changes from 1 mH to 15 mH. This figure indicates that, as L_g increases, all eigenvalues shift closer to the imaginary axis, implying a slower response. Fig. 4(b) illustrates the eigenvalue map when R_g varies from 0.5 Ω to 1.5 Ω. This figure reveals that the dominant eigenvalues λ_1 and λ_2 change slightly with R_g. However, λ_3 and λ_4 shift to the left and move away from the imaginary axis as R_g increases, indicating a faster response. However, for larger values of R_g, these eigenvalues become non-dominant, meaning that further increases in R_g have minimal impact on the transient behaviour.

Using a similar approach, the state-space representations and their matrix **A** for the conventional AHO and droop controllers are derived and reported in Appendix A. Fig. 5 compares the eigenvalue plots of EAHO, AHO, and droop control with the experimental parameters. The eigenvalues of EAHO and AHO are close, confirming their similar transient performance. In contrast, droop control exhibits dominant eigenvalues closer to the imaginary axis, which implies a slower dynamic response. This figure confirms that the proposed EAHO maintains the faster transient response characteristics of the conventional AHO compared to the droop control.

$$A = \begin{bmatrix} 2\mu_e\left(V_0^2 - 3V_{eq}^2\right) + \eta_e Q_{ref} - 2\eta_e V_{eq} F_2^* & -\eta_e V_{eq}^2 F_1^* & -\eta_e V_{eq}^2 \sin(\theta_{eq}) & \eta_e V_{eq}^2 \cos(\theta_{eq}) \\ -\eta_e F_1^* & \eta_e V_{eq} F_2^* & -\eta_e V_{eq} \cos(\theta_{eq}) & -\eta_e V_{eq} \sin(\theta_{eq}) \\ \dfrac{\cos(\theta_{eq})}{L_T} & -\dfrac{V_{eq}\sin(\theta_{eq})}{L_T} & -\dfrac{R_T}{L_T} & \omega_{eq} \\ \dfrac{\sin(\theta_{eq})}{L_T} & \dfrac{V_{eq}\cos(\theta_{eq})}{L_T} & -\omega_{eq} & -\dfrac{R_T}{L_T} \end{bmatrix} \tag{25}$$

$$F_1^* = I_d\cos(\theta_{eq}) + I_q\sin(\theta_{eq}), \quad F_2^* = I_d\sin(\theta_{eq}) - I_q\cos(\theta_{eq})$$

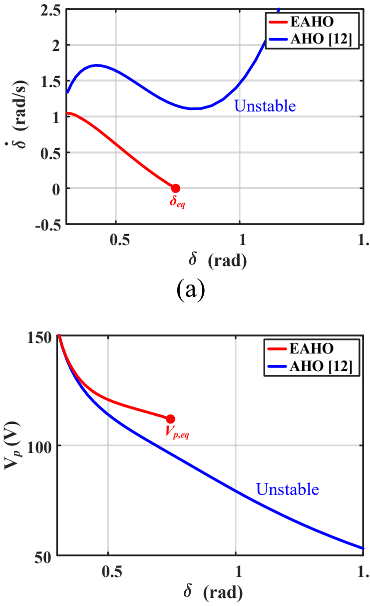

(a)

(b)

Fig. 6. (a) Phase portrait and (b) V_p-δ curves when grid voltage drops to 0.6 pu.

E. Step-by-step parameter design

In this section, a straightforward design algorithm is provided, considering both droop functionality and stability margins:

1) **Define system requirements:**
- Rated power of the inverter (P_0 and Q_0)
- Maximum allowable frequency deviation ($\Delta\omega_{max}$)
- Maximum allowable voltage amplitude ($V_{p,max}$)

2) **Calculate initial control parameters to satisfy droop requirements:**

Use (12) to compute η_e and μ_e. For the experimental parameters, these values are $\eta_e = 0.0016$ and $\mu_e = 1.16\times10^{-4}$.

3) **Check the small-signal stability for the calculated η_e and μ_e:**

From the eigenvalue map, for the system to remain stable:
- $\eta_e < \eta_{e,cr} = 0.0062 \approx 0.04$ pu, which is satisfied (if not, η_e must be curtailed to 0.0062).
- $0 < \mu_e$, which is always satisfied.

F. Large-Signal Stability Analysis

For nonlinear large-signal stability analysis of GFM inverters, two common approaches are the phase-portrait method [27] and the Lyapunov direct method [28]. The phase-portrait method is particularly useful for visualising the nonlinear evolution of system trajectories and the effect of controller dynamics on equilibrium attraction, while the Lyapunov direct method provides a more formal nonlinear stability certificate. In this work, the phase-portrait method is employed to analyse and compare the transient stability of the conventional AHO and the proposed EAHO, since it offers clear physical insight into their nonlinear behaviour.

The nonlinear dynamic equations of EAHO are presented in (14) and (15). By numerically solving these nonlinear equations in MATLAB, the trajectories $\dot{\delta} - \delta$ and $V_p - \delta$ are obtained and compared with those of the conventional AHO controller.

TABLE II

COMPARISON BETWEEN DIFFERENT VOC STRATEGIES

VOC	DZO [28]	VDPO [11]	VDPO [30]	AHO [12]	EAHO
Droop Functionality	✓	✓	✓	✓	✓
Dispatchable	×	×	✓	✓	✓
Harmonic-free waveforms	×*	×*	×*	✓	✓
Voltage-independent m_p	× $m_p = \frac{K_i K_v}{2CV^2}$	× $m_p = \frac{K_i K_v}{2CV^2}$		× $m_p = \frac{\eta}{V^2}$	✓ $m_p = \eta_e$

* The third harmonic magnitude in DZO and VDPO varies with control parameters [29].

Because grid faults may lead to high current levels and the laboratory setup has limited fault-handling capability, the transient stability analysis is performed at half of the nominal voltage and current values specified in Table I, with L_g=15 mH.

Fig. 6 presents the $\dot{\delta} - \delta$ and $V_p - \delta$ trajectories when the grid voltage drops to 0.6 pu. In this case, the proposed EAHO strategy stabilises at a new equilibrium point of (δ_{eq}, $V_{p,eq}$) = (0.74 rad, 112 V). In contrast, as shown in Fig. 6(a), the AHO response diverges, with $\dot{\delta} > 0$ for all δ, indicating that no stable equilibrium exists in the power angle trajectory.

This enhanced stability is primarily attributed to the improved reactive power support provided by the proposed strategy. According to (7) and (13), the RPL droop coefficient m_q remains always positive in EAHO, whereas it becomes negative for AHO when $V_p < V_{p0}/\sqrt{2}$, which results in an enhanced transient stability of the EAHO under severe grid disturbances.

G. Comparison with other VOCs

In this section, the performance of the EAHO is compared with two well-known VOC strategies: dead-zone oscillator (DZO) and Van der Pol oscillator (VDPO).

The DZO, originally proposed in [29], is among the earliest time-domain oscillator-based GFM methods. However, it suffers from two key limitations: 1) It is not dispatchable, meaning that explicit power setpoints cannot be assigned in grid-connected operation; and 2) It introduces harmonic distortion in the voltage waveform, as already reported in [30].

The VDPO, initially developed for single-phase GFM inverters [11], also lacked dispatchability in early implementations. Although dispatchable variants have since been proposed [31], they still exhibit third-order harmonics in the output voltage, making it less suitable for grid-connected applications without additional harmonic mitigation [30].

In contrast, AHO overcomes these limitations by being fully dispatchable and capable of generating harmonic-free sinusoidal voltages [30], [32]. The proposed EAHO retains all these advantages while offering a voltage-independent active power droop coefficient. This enables improved active/reactive power support under grid disturbances, more accurate power sharing, and enhanced system stability.

A summary of this comparison is given in Table II, highlighting the superior performance of the proposed EAHO. In this table, K_i, K_v and C are the control parameters of VDPO and DZO.

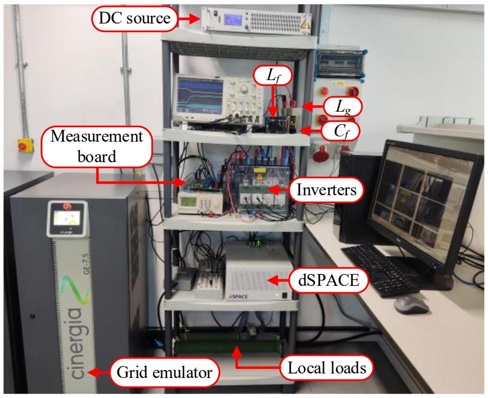

Fig. 7. Experimental test setup.

III. EXPERIMENTAL VALIDATION

To validate the theoretical findings, a 2.5 kVA test setup is implemented, as shown in Fig. 7, with parameters listed in Table I. The Cinergia 7.5 kVA grid emulator is employed to simulate the grid behaviour. The control algorithms are implemented on a dSPACE DS1007 processor. The effectiveness of the proposed strategy compared to the conventional methods is validated through seven test scenarios.

A. Scenario 1: Grid frequency change

This scenario compares the grid support capabilities in response to grid frequency variations. Here, the grid frequency decreases from 50 Hz to 49.5 Hz, with $P_{ref} = 0$ W. According to the droop performance and parameter design, the inverters are expected to inject nominal active power (2000 W). Figs. 8(a) and 9(a) compare the experimental results for the proposed EAHO and conventional AHO controllers, respectively. As shown in Fig. 8(a), the EAHO successfully inject 2000 W, whereas Fig. 9(a) shows the AHO injecting only 1800 W, 10% below the target value. This lower active power injection by AHO is consistent with Fig. 2, where its APL droop coefficient increases at the nominal voltage.

Regarding waveform quality, the total harmonic distortion (THD) of both strategies is also measured and reported in these figures. The results confirm that both voltage and current THD remain below 1% and 3%, respectively, for both strategies. This validates the harmonic-free voltage generation capability of AHO-based inverters.

B. Scenario 2: Grid voltage amplitude change

This scenario compares the inverters' reactive power support when the grid voltage first falls by 20% and then jumps by 10%, with P_{ref} and Q_{ref} set to zero. During the voltage drop to 0.8 pu, as shown in Fig. 8(b), the EAHO injects 1400 var, while Fig. 9(b) indicates that the AHO injects only 1050 var, which is 25% less than the EAHO. These results are consistent with the theoretical calculations in Section II.B, where the injected reactive powers were 1443 var and 1078 var for the EAHO and AHO, respectively. For the voltage jump to 1.1 pu, EAHO absorbs 600 var, while AHO absorbs 450 var. Both experimental and theoretical results confirm that the proposed EAHO provides approximately 25% enhanced grid support in terms of reactive power support compared to the AHO under both voltage sag and swell conditions.

C. Scenario 3: Power-sharing in stand-alone mode

In this test, both VOC-based inverters are connected in parallel with a conventional droop control inverter to supply local loads in stand-alone mode. Initially, the inverters supply a resistive load $R_{L1} = 94\ \Omega$, and then an additional load $R_{L2} = 33\ \Omega$ is added in parallel. All controllers are configured to achieve P_0 and Q_0 in response to the maximum allowable grid frequency deviation and voltage amplitude deviation.

Figs. 8(c) and 9(c) show the experimental results, where P_{EAHO}/i_{EAHO}, P_D/i_D, and P_{AHO}/i_{AHO} represent the active power/current waveforms for EAHO, conventional droop, and

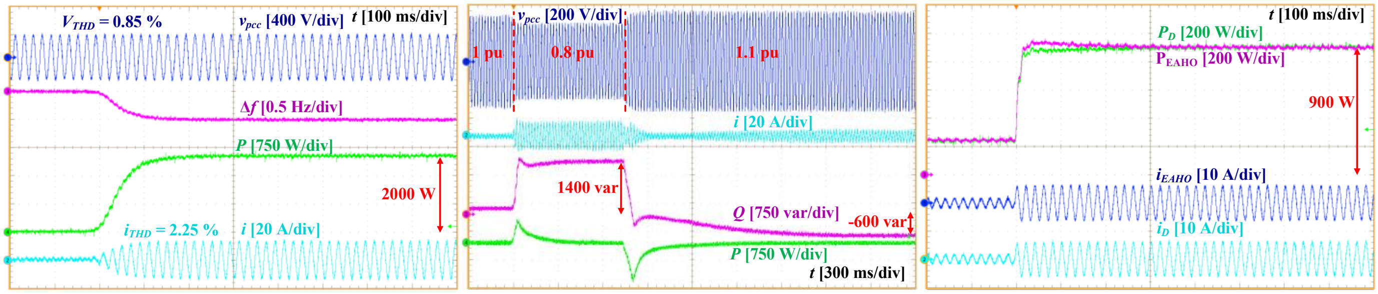

(a) (b) (c)

Fig. 8. Experimental results of EAHO: (a) Test Scenario 1, (b) Test Scenario 2, and (c) Test Scenario 3.

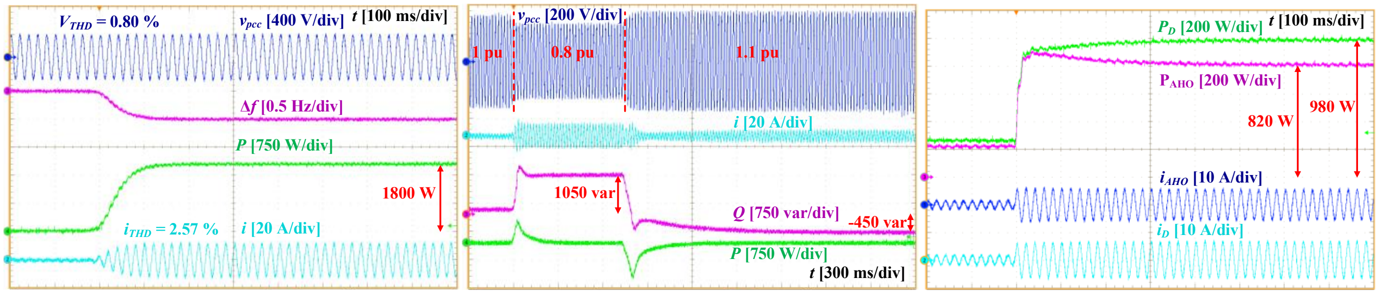

(a) (b) (c)

Fig. 9. Experimental results of AHO: (a) Test Scenario 1, (b) Test Scenario 2, and (c) Test Scenario 3.

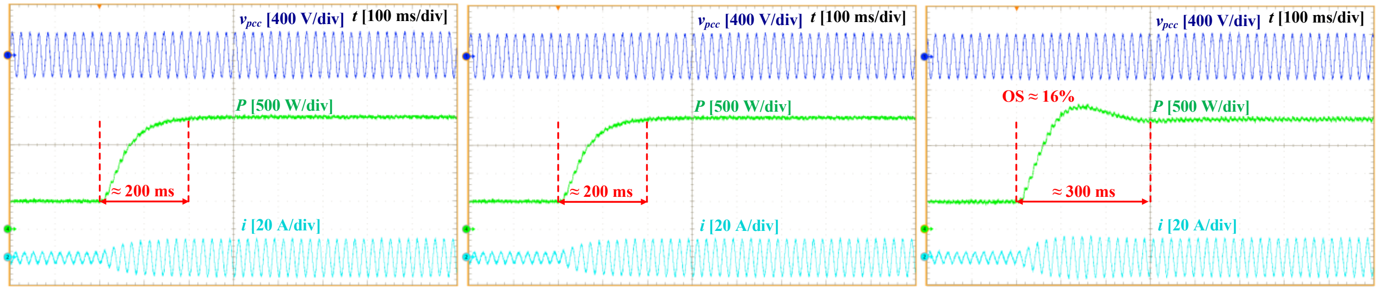

(a) (b) (c)

Fig. 10. Test Scenario 4: (a) EAHO, (b) AHO, and (c) droop control.

AHO. Fig. 8(c) illustrates the waveforms when EAHO operates in parallel with the droop control. Before and after the load change, both inverters share the active power equally, each delivering approximately 240 W and 920 W, respectively. However, for the AHO in parallel with droop control, as shown in Fig. 9(c), the active power delivered is approximately 220 W and 260 W before the load change, and about 840 W and 1000 W after the load change, respectively. This represents about a 17% power difference between the inverters, which is also reflected in the current waveforms. The results confirm the theoretical predictions in Section II.C, when EAHO, unlike conventional AHO, ensures power sharing proportional to the inverter ratings, as shown in (20) and (21).

D. Scenario 4: Active power reference change

To compare the dynamic response of different controllers, in this scenario P_{ref} changes from 500 W to 2000 W. The results, presented in Fig. 10, confirm that all strategies successfully track the reference power. Figs. 10(a) and (b) show that the proposed EAHO and the conventional AHO exhibit faster transient responses, both achieving a settling time (t_{set}) of 200 ms and without overshoot (OS). However, as shown in Fig. 10(c), droop control exhibits a slower response, with t_{set}≈300 ms and an OS of 16%. These observations are consistent with the eigenvalue comparison in Fig. 5, showing that the proposed EAHO maintains the fast transient response of AHO.

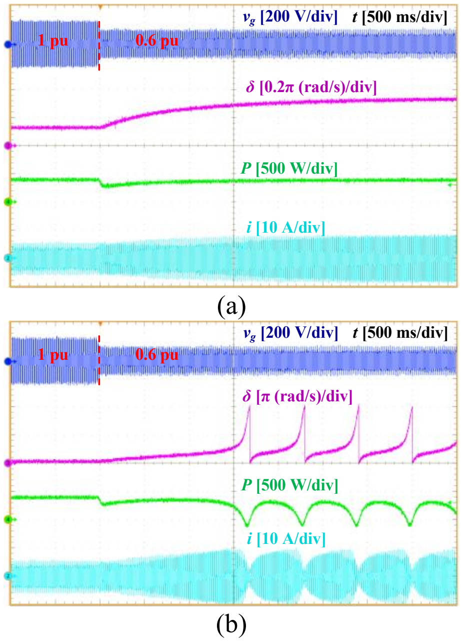

(a)

(b)

Fig. 11. Test Scenario 5: (a) EAHO and (b) AHO.

E. Scenario 5: Stability analysis under grid voltage sags

From Fig. 6, it has already been concluded that the proposed EAHO exhibits superior stability performance under severe grid voltage disturbances, owing to its always positive RPL droop coefficient. To confirm this, a test scenario is conducted for both AHO and EAHO, in which the grid voltage drops to 0.6 p.u, with the same conditions used for large-signal stability analysis in Section II.F.

Fig. 11 presents the results. Before the sag, the inverters operate with P_{ref} = 400 W. As shown in Fig. 11(a), the proposed EAHO remains stable during the disturbance. In contrast, AHO, as depicted in Fig. 11(b), fails to establish equilibrium points, preventing P from reaching its reference value. Consequently, low-frequency oscillations appear in P, δ, and i, indicating instability.

Table III compares the AHO and EAHO based on experimental results of Test Scenarios 1-5, confirming that EAHO offers better grid support capability, power-sharing accuracy, and transient stability performance compared to AHO, while preserving its transient speed.

F. Scenario 6: Grid disconnection in parallel operation

In this scenario, two inverters with EAHO controllers are connected in parallel to supply a local load (R_L=47 Ω) and the grid. Before grid disconnection, each inverter was programmed with P_{ref} = 1000 W, meaning each supplied 1000 W to the combined load and grid. Fig. 12 (a) presents the experimental results when the grid is suddenly disconnected by opening its relay, where i_g is the grid current. This figure shows that each inverter supplies 1000 W before the grid disconnection. After disconnection, the output power of both inverters shifts smoothly to 480 W to supply the local load equally. This smooth transition is evident in the zoomed-in voltage and current waveforms of Fig. 12(b). These results confirm that both inverters continued to operate without tripping, demonstrating the robustness of the proposed strategy in maintaining stable operation following grid disconnection.

TABLE III

COMPARISON BETWEEN EAHO AND AHO

GFM strategy	EAHO	AHO [12]
Active and reactive power support (Figs. 8, 9 (a),(b))	2000 W 1400 var	1800 W 1050 var
Power-sharing error (Figs. 8,9 (c))	≈ 0 %	≈ 16%
Dynamic response (t_{set} in Fig. 10)	200 ms	200 ms
Transient stability (Fig. 11)	Stable	Unstable

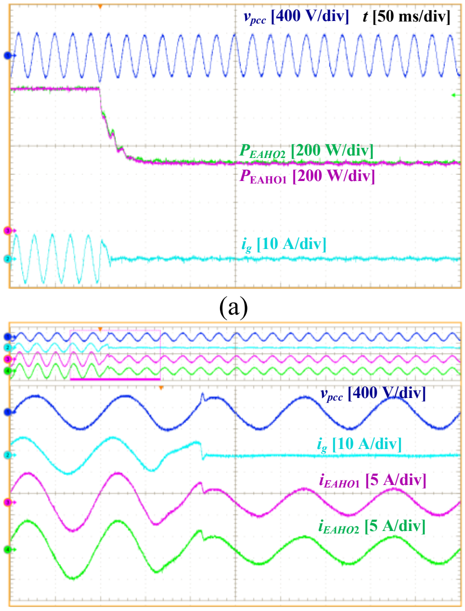

(a)

(b)

Fig. 12. Test Scenario 6: (a) EAHO parallel with EAHO and (b) zoomed view of current waveforms.

G. Scenario 7: Variation in grid impedance and control parameters

This section examines the effect of variation in control and grid impedance parameters on the EAHO's transient performance. The results are compared with those presented for the designed values in Fig. 10(a), where L_g=1 mH, R_g=1 Ω, and $\eta_e=\eta_{e,set}$=0.0016. Figs. 13(a) and (b) show the EAHO's response when P_{ref} jumps from 500 W to 2000 W under different grid impedance values. Fig. 13(a) demonstrates a significantly slower response (760 ms) when L_g is increased to 15 mH, consistent with the eigenvalue map in Fig. 4(a). In contrast, Fig. 13(b) shows only a slight change in the transient response when R_g is reduced to 0.5 Ω, which agrees with the eigenvalue map in Fig. 4(b), where the dominant eigenvalues shift only slightly with R_g. The controller's resilience against real-time grid impedance variations is further investigated in Fig. 13(c). In this test, the inverter operates at P_{ref} = 1500 W with L_g = 5 mH. Then, a 1 mH inductor is added in parallel and subsequently removed in real time, altering L_g to 0.83 mH and back. The results in Fig. 13 confirm that the steady-state performance of the EAHO is not affected by variations in grid impedance, while its transient response speed is influenced by such changes.

Fig. 14(a) shows the results for different control parameters, η_e=0.5$\eta_{e,set}$, when P_{ref} changes from 500 W to 2000 W. Comparing this figure with Fig. 10(a) reveals that active power reaches its final value within 480 ms and 200 ms for η_e=0.5$\eta_{e,set}$ and $\eta_e=\eta_{e,set}$, respectively. These results are consistent with the eigenvalue map of Fig. 3(a), in which decreasing η_e results in a slower response.

Similar to AHO, the initial synchronisation time of the EAHO is primarily influenced by μ_e. Thus, to validate the small-signal analysis, the output voltage generation time is measured for different μ_e values. Figs. 14(b) and (c) present the results, showing that the oscillator's voltage reaches its final value within 280 ms and 110 ms for $\mu_e=\mu_{e,set}$ and μ_e=4$\mu_{e,set}$, respectively. These results are consistent with the eigenvalue map in Fig. 3(b), where increasing μ_e results in a faster response.

IV. CONCLUSION

This paper introduced an enhanced AHO control strategy for grid-forming inverters that overcomes the inherent limitations of the conventional AHO. By applying a simple yet effective modification to the current error feedback term, the proposed

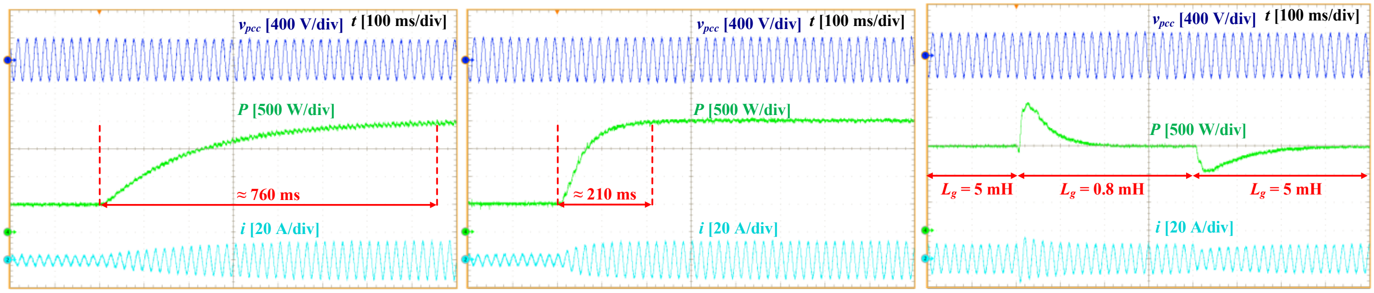

(a) (b) (c)

Fig. 13. Test Scenario 7 under grid impedance variations: (a) L_g=15 mH, R_g=1 Ω, (b) L_g=1 mH, R_g=0.5 Ω, and (c) sudden changes in L_g.

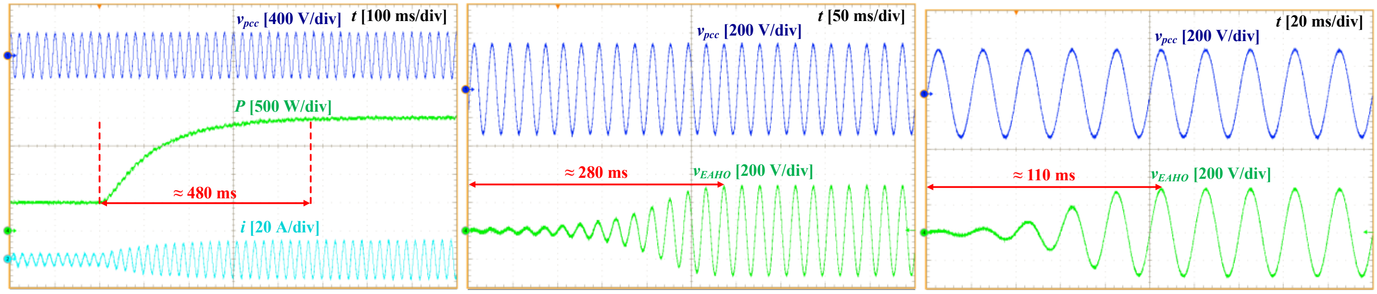

(a) (b) (c)

Fig. 14. Test Scenario 7 under different control parameters: (a) η_e=0.5$\eta_{e,set}$, $\mu_e=\mu_{e,set}$, (b) $\eta_e=\eta_{e,set}$, $\mu_e=\mu_{e,set}$, and (c) $\eta_e=\eta_{e,set}$, μ_e=4$\mu_{e,set}$.

$$A=\begin{bmatrix} 2\mu\left(V_0^2-3V_{eq}^2\right)-\dfrac{\eta Q_{ref}}{V_{eq}^2} & -\eta F_1^* & -\eta\sin(\theta_{eq}) & \eta\cos(\theta_{eq}) \\ -2\dfrac{\eta}{V_{eq}^3}P_{ref}+\dfrac{\eta}{V_{eq}^2}F_1^* & \dfrac{\eta}{V_{eq}}F_2^* & -\dfrac{\eta}{V_{eq}}\cos(\theta_{eq}) & -\dfrac{\eta}{V_{eq}}\sin(\theta_{eq}) \\ \dfrac{\cos(\theta_{eq})}{L_T} & -\dfrac{V_{eq}\sin(\theta_{eq})}{L_T} & -\dfrac{R_T}{L_T} & \omega_{eq} \\ \dfrac{\sin(\theta_{eq})}{L_T} & \dfrac{V_{eq}\cos(\theta_{eq})}{L_T} & -\omega_{eq} & -\dfrac{R_T}{L_T} \end{bmatrix} \tag{26}$$

$$A=\begin{bmatrix} -\omega_q(1+m_qF_2^*) & -m_q\omega_qV_{eq}F_1^* & 0 & -m_q\omega_qV_{eq}\sin(\theta_{eq}) & m_q\omega_qV_{eq}\cos(\theta_{eq}) \\ 0 & 0 & 1 & 0 & 0 \\ -m_p\omega_pF_1^* & m_p\omega_pF_2^* & -\omega_p & -m_p\omega_pV_{eq}\cos(\theta_{eq}) & -m_p\omega_pV_{eq}\sin(\theta_{eq}) \\ \dfrac{\cos(\theta_{eq})}{L_T} & -\dfrac{V_{eq}\sin(\theta_{eq})}{L_T} & I_q & -\dfrac{R_T}{L_T} & \omega_{eq} \\ \dfrac{\sin(\theta_{eq})}{L_T} & \dfrac{V_{eq}\cos(\theta_{eq})}{L_T} & -I_d & -\omega_{eq} & -\dfrac{R_T}{L_T} \end{bmatrix} \tag{27}$$

approach achieves a linear, voltage-independent active power droop coefficient while preserving the original AHO structure, harmonic-free voltage generation, and fast transient dynamics.

Comprehensive large-signal and small-signal analyses demonstrated that the EAHO provides improved active and reactive power support, enhanced droop characteristics, and superior stability margins under grid voltage and frequency variations. Experimental results obtained from a 2.5 kVA single-phase inverter platform validated the theoretical findings, confirming accurate power sharing in parallel operation, improved frequency and voltage support during disturbances, and stable operation under severe voltage sags where the conventional AHO becomes unstable.

Despite these advancements, the proposed EAHO strategy does not, in its current form, encompass all functionalities required for comprehensive ancillary service provision. In addition, although the present paper has demonstrated transient-stability enhancement using large-signal phase-portrait analysis, a formal Lyapunov direct-method-based analysis would provide an additional nonlinear stability certificate. Therefore, future work will focus on extending the proposed strategy toward broader ancillary-service functionality and on developing a Lyapunov-based nonlinear stability framework for VOC-based GFM inverters.

APPENDIX A

The Jacobian matrices for the AHO and droop control are given in (26) and (27), respectively, where state variables for the AHO are $\Delta x=[\Delta v, \Delta\theta, \Delta i_d, \Delta i_q]^T$ and for the droop control are $\Delta x=[\Delta v, \Delta\theta, \Delta\omega, \Delta i_d, \Delta i_q]^T$, and F_1^* and F_2^* are given in (25).

REFERENCES

[1] N. Pogaku, M. Prodanovic, and T. C. Green, "Modeling, Analysis and Testing of Autonomous Operation of an Inverter-Based Microgrid," *IEEE Trans. Power Electron.*, vol. 22, no. 2, pp. 613–625, Mar. 2007, doi: 10.1109/TPEL.2006.890003.

[2] J. Driesen and K. Visscher, "Virtual synchronous generators," *IEEE Power Energy Soc. 2008 Gen. Meet. Convers. Deliv. Electr. Energy 21st Century, PES*, pp. 26–28, 2008, doi: 10.1109/PES.2008.4596800.

[3] K. M. Cheema, "A comprehensive review of virtual synchronous generator," *Int. J. Electr. Power Energy Syst.*, vol. 120, no. February, p. 106006, 2020, doi: 10.1016/j.ijepes.2020.106006.

[4] Q. C. Zhong and G. Weiss, "Synchronverters: Inverters that mimic synchronous generators," *IEEE Trans. Ind. Electron.*, vol. 58, no. 4, pp. 1259–1267, 2011, doi: 10.1109/TIE.2010.2048839.

[5] Qing-Chang Zhong, Phi-Long Nguyen, Zhenyu Ma, and Wanxing Sheng, "Self-Synchronized Synchronverters: Inverters Without a Dedicated Synchronization Unit," *IEEE Trans. Power Electron.*, vol. 29, no. 2, pp. 617–630, Feb. 2014, doi: 10.1109/TPEL.2013.2258684.

[6] W. Zhang, A. M. Cantarellas, J. Rocabert, A. Luna, and P. Rodriguez, "Synchronous Power Controller With Flexible Droop Characteristics for Renewable Power Generation Systems," *IEEE Trans. Sustain. Energy*, vol. 7, no. 4, pp. 1572–1582, Oct. 2016, doi: 10.1109/TSTE.2016.2565059.

[7] M. Sinha, F. Dorfler, B. B. Johnson, and S. V. Dhople, "Uncovering droop control laws embedded within the nonlinear dynamics of van der pol oscillators," *IEEE Trans. Control Netw. Syst.*, vol. 4, no. 2, pp. 347–358, 2017, doi: 10.1109/TCNS.2015.2503558.

[8] H. Yu, M. A. Awal, H. Tu, I. Husain, and S. Lukic, "Comparative Transient Stability Assessment of Droop and Dispatchable Virtual Oscillator Controlled Grid-Connected Inverters," *IEEE Trans. Power Electron.*, vol. 36, no. 2, pp. 2119–2130, Feb. 2021, doi: 10.1109/TPEL.2020.3007628.

[9] Z. Shi, J. Li, H. I. Nurdin, and J. E. Fletcher, "Comparison of Virtual Oscillator and Droop Controlled Islanded Three-Phase Microgrids," *IEEE Trans. Energy Convers.*, vol. 34, no. 4, pp. 1769–1780, 2019, doi: 10.1109/TEC.2019.2922447.

[10] B. Johnson, M. Rodriguez, M. Sinha, and S. Dhople, "Comparison of virtual oscillator and droop control," in *2017 IEEE 18th Workshop on Control and Modeling for Power Electronics (COMPEL)*, IEEE, Jul. 2017, pp. 1–6. doi: 10.1109/COMPEL.2017.8013298.

[11] B. B. Johnson, M. Sinha, N. G. Ainsworth, F. Dorfler, and S. V. Dhople, "Synthesizing Virtual Oscillators to Control Islanded Inverters," *IEEE Trans. Power Electron.*, vol. 31, no. 8, pp. 6002–6015, Aug. 2016, doi: 10.1109/TPEL.2015.2497217.

[12] M. A. Awal and I. Husain, "Unified Virtual Oscillator Control for Grid-Forming and Grid-Following Converters," *IEEE J. Emerg. Sel. Top. Power Electron.*, vol. 9, no. 4, pp. 4573–4586, Aug. 2021, doi: 10.1109/JESTPE.2020.3025748.

[13] H. Rezazadeh, M. Monfared, M. Fazeli, and S. Golestan, "Virtual Oscillator Control for Grid-Forming Inverters: Recent Advances, Comparative Evaluation, and Small-Signal Analysis," *Energies*, vol. 18, no. 22, p. 5981, Nov. 2025, doi: 10.3390/en18225981.

[14] M. Lu, "Virtual Oscillator Grid-Forming Inverters: State of the Art, Modeling, and Stability," *IEEE Trans. Power Electron.*, vol. 37, no. 10, pp. 11579–11591, Oct. 2022, doi: 10.1109/TPEL.2022.3163377.

[15] S. Luo, W. Chen, X. Li, and Z. Hao, "A New Virtual Inertial Strategy for Andronov–Hopf Oscillator Based Grid-Forming Inverters," *IEEE J. Emerg. Sel. Top. Power Electron.*, vol. 12, no. 2, pp. 1995–2005, Apr. 2024, doi: 10.1109/JESTPE.2024.3370171.

[16] H. Rezazadeh, M. Monfared, M. Fazeli, and S. Golestan, "Providing Inertial Response with Unified VOC for Single-phase GFM Inverters," in *2024 International Symposium on Electrical, Electronics and Information Engineering (ISEEIE)*, IEEE, Aug. 2024, pp. 94–98. doi: 10.1109/ISEEIE62461.2024.00025.

[17] H. Rezazadeh, M. Monfared, M. Fazeli, and S. Golestan, "Enhancing Damping in Single-Phase Grid-Forming Virtual Oscillator Control Inverters: A Feedforward Strategy," *IEEE Open J. Ind. Electron. Soc.*, vol. 6, no. July, pp. 1101–1115, 2025, doi: 10.1109/OJIES.2025.3588677.

[18] S. Luo, W. Chen, H. Jin, Y. Wang, and Z. Hao, "Voltage Feedforward Damping Control Based on Duffing–Hopf Oscillator for Parallel Grid-Forming Inverters," *IEEE Trans. Power Electron.*, vol. 40, no. 9, pp. 13703–13715, Sep. 2025, doi: 10.1109/TPEL.2025.3568790.

[19] Z. Zeng, J. Fan, Y. Sun, S. Wang, and D. Yang, "A Dispatchable Virtual Oscillator Controller in the dq Frame With Enhanced Grid-Forming Power Reference Tracking Capability," *IEEE Trans. Power Electron.*, vol. 40, no. 8, pp. 10973–10987, Aug. 2025, doi: 10.1109/TPEL.2025.3556325.

[20] J. Wang, S. Ganguly, S. Chakraborty, and B. Kroposki, "Performance Evaluation of a Single-Phase Grid-Forming Inverter Through Hardware Experiments," in *2024 IEEE Energy Conversion Congress and Exposition (ECCE)*, IEEE, Oct. 2024, pp. 1498–1505. doi: 10.1109/ECCE55643.2024.10861136.

[21] H. Rezazadeh, M. Monfared, M. Fazeli, and S. Golestan, "Single-phase Grid-forming Inverters: A Review," in *2023 International Conference on Computing, Electronics & Communications Engineering (iCCECE)*, IEEE, Aug. 2023, pp. 7–10. doi: 10.1109/iCCECE59400.2023.10238661.

[22] U. C. Nwaneto and A. M. Knight, "Using Dynamic Phasors To Model and Analyze Selective Harmonic Compensated Single-Phase Grid-Forming Inverter Connected to Nonlinear and Resistive Loads," *IEEE Trans. Ind. Appl.*, vol. 59, no. 5, pp. 6136–6154, Sep. 2023, doi: 10.1109/TIA.2023.3282925.

[23] J. A. Suul, S. DArco, and G. Guidi, "Virtual Synchronous Machine-Based Control of a Single-Phase Bi-Directional Battery Charger for Providing Vehicle-to-Grid Services," *IEEE Trans. Ind. Appl.*, vol. 52, no. 4, pp. 3234–3244, Jul. 2016, doi: 10.1109/TIA.2016.2550588.

[24] S. Luo, W. Chen, Z. Hao, and Y. Wang, "A Transient Stability Enhanced Andronov-Hopf Oscillator for Grid-Forming Converters," *IEEE Trans. Power Electron.*, vol. 39, no. 9, pp. 10853–10864, Sep. 2024, doi: 10.1109/TPEL.2024.3404426.

[25] S. Singh, A. R. Gautam, and D. Fulwani, "Constant power loads and their effects in DC distributed power systems: A review," *Renew. Sustain. Energy Rev.*, vol. 72, no. December 2015, pp. 407–421, May 2017, doi: 10.1016/j.rser.2017.01.027.

[26] National Grid, THE GRID CODE, National Grid, 2025. https://dcm.nationalenergyso.com/

[27] D. Pan, X. Wang, F. Liu, and R. Shi, "Transient Stability of Voltage-Source Converters With Grid-Forming Control: A Design-Oriented Study," *IEEE J. Emerg. Sel. Top. Power Electron.*, vol. 8, no. 2, pp. 1019–1033, Jun. 2020, doi: 10.1109/JESTPE.2019.2946310.

[28] M. Al Talaq, M. B. Abdelghany, A. Al-Durra, H. Zeineldin, and T. EL-Fouly, "A Sophisticated Grid-Forming Dispatchable-Virtual Oscillator Control With Robust Inner Current Control for Improving Transient Stability," *IEEE Trans. Power Electron.*, vol. 40, no. 10, pp. 15064–15079, Oct. 2025, doi: 10.1109/TPEL.2025.3575573.

[29] B. B. Johnson, S. V. Dhople, A. O. Hamadeh, and P. T. Krein, "Synchronization of parallel single-phase inverters with virtual oscillator control," *IEEE Trans. Power Electron.*, vol. 29, no. 11, pp. 6124–6138, 2014, doi: 10.1109/TPEL.2013.2296292.

[30] M. Lu, S. Dhople, and B. Johnson, "Benchmarking Nonlinear Oscillators for Grid-Forming Inverter Control," *IEEE Trans. Power Electron.*, vol. 37, no. 9, pp. 10250–10266, Sep. 2022, doi: 10.1109/TPEL.2022.3162530.

[31] M. A. Awal, H. Yu, H. Tu, S. M. Lukic, and I. Husain, "Hierarchical Control for Virtual Oscillator Based Grid-Connected and Islanded Microgrids," *IEEE Trans. Power Electron.*, vol. 35, no. 1, pp. 988–1001, Jan. 2020, doi: 10.1109/TPEL.2019.2912152.

[32] H. Rezazadeh, M. Monfared, M. Fazeli, and S. Golestan, "Virtual Oscillator Control for Grid-Forming Inverters: An Overview of Recent Developments and Small-Signal Analysis," in *2025 Energy Conversion Congress & Expo Europe (ECCE Europe)*, IEEE, Sep. 2025, pp. 1–6. doi: 10.1109/ECCE-Europe62795.2025.11238644.

Hamed Rezazadeh received the B.Sc. and M.Sc. degrees (Hons.) in electrical engineering from Ferdowsi University of Mashhad, Mashhad, Iran, in 2017 and 2020, respectively. He is currently working toward his PhD degree in power electronics at Swansea University, Swansea, U.K. His research interests include power electronics, renewable energy systems, and grid-forming inverters. Mr Rezazadeh is an active reviewer for various IEEE TRANSACTIONS.

Mohammad Monfared (Senior Member, IEEE) received the M.Sc. and PhD degrees (Hons.) in electrical engineering from Amirkabir University of Technology, Tehran, Iran, in 2006 and 2010, respectively. Since 2022, he has been a Senior Lecturer with the Faculty of Science and Engineering, Swansea University, Swansea, U.K. His research interests include power electronics, renewable energy systems, and energy management. Dr Monfared is an Associate Editor of IEEE TRANSACTIONS ON INDUSTRIAL ELECTRONICS and IEEE TRANSACTIONS ON POWER ELECTRONICS, and a member of IEEE IES Technical Committee on Renewable Energy Systems (TC-RES).

Meghdad Fazeli (Senior Member, IEEE) received the M.Sc. and PhD degrees from the University of Nottingham, U.K., in 2006 and 2011, respectively. In September 2013, he became an Academic Staff member with the Electronic and Electrical Engineering Department, Swansea University, where he is currently a Senior Lecturer. His main research interests include integration and control of renewable energy, ancillary services, VSMs, energy management systems, and micro/ nano-grids.

Saeed Golestan (Senior Member, IEEE) received the PhD degree in electrical engineering from Aalborg University, Aalborg, Denmark, in 2018. He is currently an Associate Professor with AAU Energy, Aalborg University. His research interests include modelling, synchronisation, and control of power electronic converters and microgrids for renewable energy systems. He is an Associate Editor for IEEE TRANSACTIONS ON POWER ELECTRONICS, IEEE TRANSACTIONS ON INDUSTRIAL ELECTRONICS, IEEE OPEN JOURNAL OF THE INDUSTRIAL ELECTRONICS SOCIETY, and IEEE JOURNAL OF EMERGING AND SELECTED TOPICS IN POWER ELECTRONICS. He was the recipient of several awards, including the 2023 IEEE TPE Associate Editor Excellence Award and the 2022 Energies Young Investigator Award.